ACS APPLIED MATERIALS & INTERFACES

www.acsami.org Research Article

$LiAlO_2/LiAl_5O_8$ Membranes Derived from Flame-Synthesized Nanopowders as a Potential Electrolyte and Coating Material for All-Solid-State Batteries

Eleni Temeche, Sylvio Indris, and Richard M. Laine*

Cite This: *ACS Appl. Mater. Interfaces* 2020, 12, 46119–46131 Read Online

ACCESS | Metrics & More | Article Recommendations | Supporting Information

ABSTRACT: Recently, γ-$LiAlO_2$ has attracted considerable attention as a coating in Li-ion battery electrodes. However, its potential as a Li^+ ceramic electrolyte is limited due to its poor ionic conductivity ($<10^{-10}$ S cm^{-1}). Here, we demonstrate an effective method of processing $LiAlO_2$ membranes (<50 μm) using nanopowders (NPs) produced via liquid-feed flame spray pyrolysis (LF-FSP). Membranes consisting of selected mixtures of lithium aluminate polymorphs and Li contents were processed by conventional tape casting of NPs followed by thermocompression of the green films (100 °C/10 kpsi/10 min). The sintered green films (1100 °C/2 h/air) present a mixture of $LiAlO_2$ (~72 wt %) and $LiAl_5O_8$ (~27 wt %) phases, offering ionic conductivities ($>10^{-6}$ S cm^{-1}) at ambient with an activation energy of 0.5 eV. This greatly increases their potential utility as ceramic electrolytes for all-solid-state batteries, which could simplify battery designs, significantly reduce costs, and increase their safety. Furthermore, a solid-state $Li/Li_{3.1}AlO_2/Li$ symmetric cell was assembled and galvanostatically cycled at 0.375 mA cm^{-2} current density, exhibiting a transference number ≈ 1.

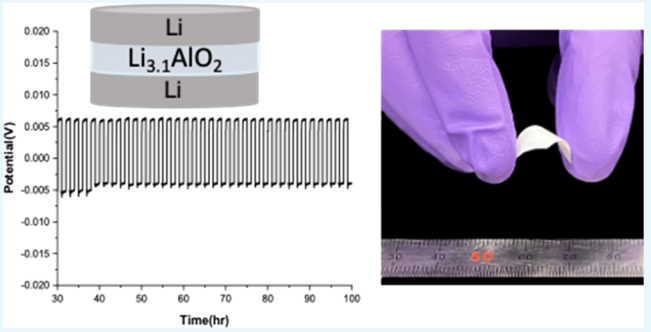

KEYWORDS: *nanopowders, coatings, ceramic electrolyte, $LiAlO_2$, $LiAl_5O_8$*

1. INTRODUCTION

Lithium-ion batteries (LIBs) used for portable devices are now being commercialized at large scales (e.g., electric and hybrid electric vehicles) due to their high energy and power densities, cyclability, and high operating voltages.[1] Unfortunately, current LIBs using liquid electrolytes still suffer from limited electrochemical performance, poor thermal stabilities, low ion selectivity, and flammability.[2] The replacement of liquid electrolytes with solid electrolytes will resolve the fundamental safety issues due to their nonflammability and high thermal stabilities, thereby offering access to new battery chemistries and designs.[3]

Ceramic Li^+ superionic conductors (0.1−1 mS cm^{-1})[4] with rigid skeletal structures, low activation energies (<0.4 eV),[5] low electronic conductivities ($<1 \times 10^{-8}$ S cm^{-1}),[6] and thermal stability are proposed to improve battery chemistries and increase energy densities by eliminating peripheral mass and reducing battery pack size.[7] Solid electrolytes with garnet-type c-LLZO ($Li_7La_3Zr_2O_{12}$),[8] NASICON [$Li_{1+x}Al_xTi_{2-x}(PO_4)_3$],[9] and perovskite ($La_{3x}La_{2/3-x}TiO_3$)[10] crystal structures have been engineered to increase Li^+ conductivity by modifying conduction pathways through aliovalent substitution, optimizing Li^+ vacancy sites and concentrations of mobile species.[11−14] However, little attention has been given to lithium aluminate polymorphs as ceramic Li^+ conductors due to their poor ambient ionic conductivities ($<10^{-10}$ S cm^{-1}), which can be compensated for, as with LiPON ($Li_xPO_yN_z$),[15] through the use of thin, defect-free, and dense films.[6,16]

$LiAlO_2$ has been reported to be a good candidate for carbonate fuel cells as an electrolyte matrix,[17] as a substrate for growing GaN epitaxial film,[18] and as a catalyst for biodiesel production.[19] $LiAlO_2$ has also been used as a ceramic filler for polymer electrolytes.[20] Recently, $LiAlO_2$ has been explored as a potential ceramic electrolyte for assembling solid-state microbatteries because of its chemical and thermal stability.[6] In addition to its potential use as a solid-state electrolyte, polymorphs of lithium aluminates have been studied as coatings for LIB electrodes.[16]

The reactivity of LIB electrodes with $LiPF_6$-based electrolytes results in corrosive dissolution of redox-active species from the active materials, which can be suppressed by introducing a coating as a physical protective barrier.[16] The

Received: July 21, 2020
Accepted: September 16, 2020
Published: September 16, 2020

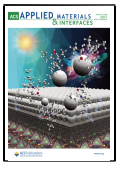

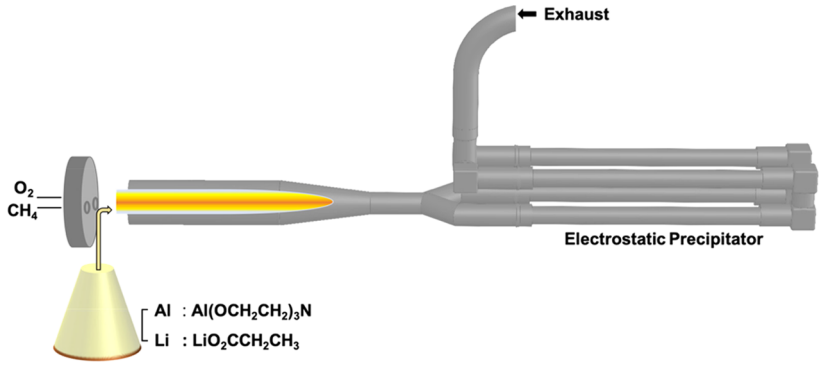

Figure 1. Schematic of LF-FSP apparatus.

most promising coating materials (Al_2O_3,[12] ZnO,[21] $LiAlO_2$,[16] and Li_2ZrO_3[22]) are expected to offer new opportunities for next-generation all-solid-state batteries (ASSBs) as intermediate buffers and wetting agents. Recently, $LiAl_5O_8$ was found to form in an alumina-coated garnet LLCZN ($Li_7La_{2.75}Ca_{0.25}Zr_{1.75}Nb_{0.25}O_{12}$) interface with a Li metal anode. The effect was to reduce interfacial impedance.[12] This implies that formation of lithiated alumina ($LiAl_5O_8$) improves Li^+ migration through the ceramic electrolyte/Li interface.[12]

Different synthesis approaches have targeted processing single-phase $LiAlO_2$ membranes with desirable morphological and conductive features.[23] Some of the pathways assessed include solid-state,[19] hydrothermal,[24] sol−gel,[25] combustion,[26] and atomic layer deposition (ALD) synthesis methods.[27] Recently, Hu et al. described ALD processing $LiAlO_2$ films 90, 160, and 235 nm-thick on different substrates with ambient conductivities of 10^{-10} S cm^{-1} and average activation energies of 0.8 eV.[6]

The fabrication of these extremely thin films requires gas-phase deposition techniques. However, the exploration of Li^+ conductive thin-film electrolytes by gas-phase deposition techniques, such as ALD,[6] ion beam-assisted deposition,[28] and pulse laser deposition,[29] is still at an early stage as such methods are energy and equipment intensive, require high-cost process steps, and offer low deposition rates.[30] Thus, there remains a considerable need to develop alternate methods of processing membranes with optimal conductivity as potential candidates for next generation ASSBs.

Recent developments in microelectronic industries have reduced the energy and power density requirements of electronic devices.[31] Hence, thin-film microbatteries delivering capacities in the range of 0.1−5 mAh can be used as power sources for these devices.[32] These microbatteries provide various advantages such as low internal resistance, and excellent rechargeability and enable simple designs in ultrathin watches, computer memory chips, and microsensors.[31,33] Typically, microbatteries are assembled using thin solid electrolytes (∼1 μm) with the full stack in the range of 10−15 μm-thick.[32] However, the presence of a substrate is reported to at least double the overall battery thickness.[32] The main challenges of thin-film batteries are finding thin, lightweight substrates to support the battery and protect lithium metal and lithium-containing electrodes from air exposure.[32,34] The development of a thin-film battery on flexible substrates has been suggested to improve the energy storage capacity per unit weight and allow the use of special designs.[34] In our previous work, we demonstrated that LF-FSP NPs enable the formation of flexible and dense Al_2O_3 membranes with an average thickness of <10 μm.[7,35] For conventional microbatteries, thin-film electrolytes with room-temperature conductivities >10^{-6} S cm^{-1} are highly desirable.[36] Thus, this provides the motivation to develop the Li^+ conducting membrane that can potentially serve as both the electrolyte and substrate for such batteries.

The present study aims to demonstrate an effective alternate method of processing $LiAlO_2$ membranes (<50 μm) using high surface area, flame-made NPs produced via LF-FSP, which eliminates traditional solid-state reaction steps (i.e., crushing and ball milling).[37] $LiAlO_2$ membranes are produced by tape casting the NP/polymeric binder slurries followed by thermocompression of green films (100 °C/10 kpsi/10 min) and sintering at the desired temperature to obtain fully dense (>95%) films.

Here, we also demonstrate optimization of Li^+ conductivity in $LiAlO_2$ membranes through careful engineering of grain boundary properties by introducing a second phase ($LiAl_5O_8$) and modifying sintering conditions to minimize grain boundary resistance. Mixed phases of $LiAlO_2$ and $LiAl_5O_8$ offer superior ionic conductivities (∼10^{-6} S cm^{-1}) at ambient conditions, greatly increasing their potential utility as ceramic electrolytes that may greatly simplify ASSB designs and significantly reduce costs. These $LiAlO_2$/$LiAl_5O_8$ membranes offer potential utility as ceramic electrolytes in thin-film microbatteries and coating materials for LIB electrodes. Sintered $LiAlO_2$/$LiAl_5O_8$ and $LiAlO_2$ membranes were characterized by XRD, SEM, $^7Li/^{27}Al$ NMR, and EIS. Coincidently, we explored the stability of the $LiAlO_2$/$LiAl_5O_8$ membrane when assembled in a symmetric cell with metallic Li.

2. EXPERIMENTAL SECTION

2.1. $LiAlO_2$ Powder Synthesis. Lithium propionate [$LiO_2CCH_2CH_3$] and alumatrane [$Al(OCH_2CH_2)_3N$] were synthesized as described previously.[9] $LiAlO_2$ NPs were produced using LF-FSP, as shown in Figure 1. Lithium propionate and alumatrane were quantitatively mixed at selected molar ratios to result in $LiAlO_2$ composition with 60, 80, 150, and 300 wt % excess lithium, hereafter referred to as $Li_{1.72}AlO_2$, $Li_{1.99}AlO_2$, $Li_{3.1}AlO_2$, and $Li_{6.2}AlO_2$, respectively. Previous studies show that resulting NPs are Li deficient arising from Li_2O volatility at flame temperatures >1000 °C.[7,9]

Hence, excess lithium propionate was introduced to promote formation of the phase pure material. The resulting precursor mixture was dissolved in ethanol to give a 3 wt % ceramic yield solution. The LF-FSP was ignited using CH_4/O_2 pilot torches. Flame spray pyrolysis was then initiated by injecting the precursor solution aerosol into the combustion chamber (1.5 m long). After combustion

https://dx.doi.org/10.1021/acsami.0c13021
ACS Appl. Mater. Interfaces 2020, 12, 46119−46131

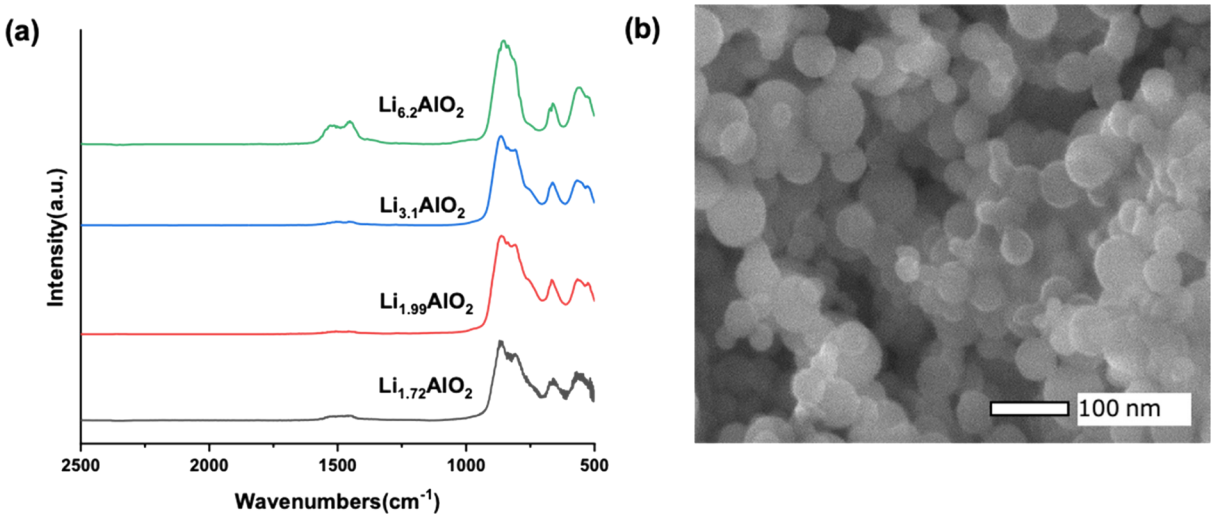

Figure 2. (a) FTIR spectra and (b) SEM image of a typical as-produced $Li_{6.2}AlO_2$ NP.

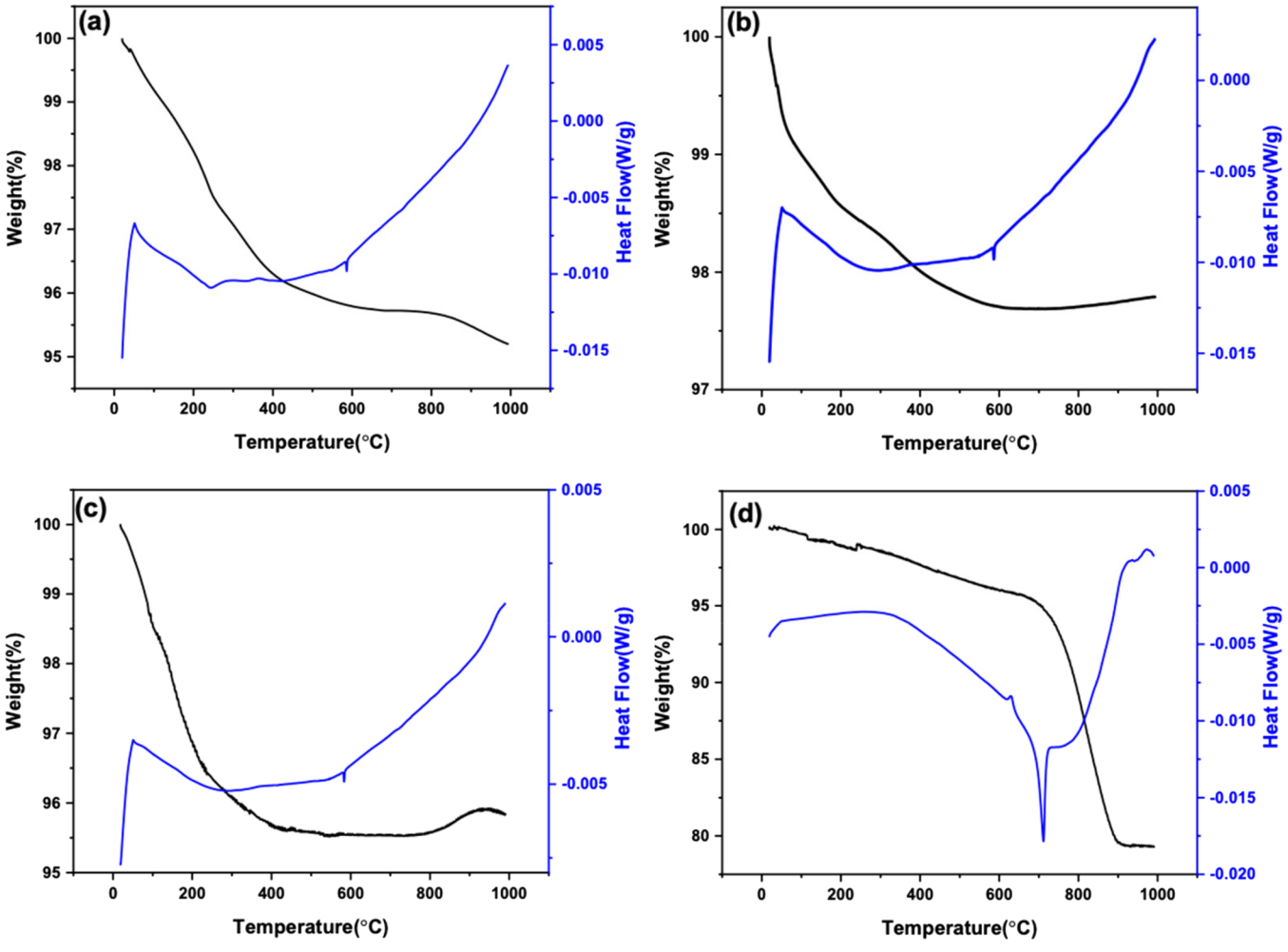

Figure 3. (a–d) TGA–DTA (1000 °C/air) of as-produced $LiAlO_2$ NPs. (a) $Li_{1.75}AlO_2$, (b) $Li_{1.99}AlO_2$, (c) $Li_{3.1}AlO_2$, and (d) $Li_{6.2}AlO_2$.

and rapid quenching, as-produced NPs were collected downstream in a parallel set of electrostatic precipitators (ESPs) operated between 5 and 10 kV. Table S1 lists the amount of lithium and aluminum precursors used to produce the NPs with varying compositions.

An ultrasonic horn (Vibra-Cell VC 505, Sonics & Materials, Inc.) operating at 100 W for 10–15 min was used to disperse the as-produced $LiAlO_2$ NPs (10 g, 0.15 mol) in anhydrous ethanol (350 mL). Polyacrylic acid (200 mg, 1.2 mmol) was used as a dispersant. Thereafter, the dispersed solution was left to settle for 4 h. The supernatant was decanted, and the recovered NPs were dried at 60 °C/12 h.

2.2. $LiAlO_2$ Membrane Synthesis. Table S2 lists the components used for formulating $LiAlO_2$ films. Briefly, the $LiAlO_2$ NPs were mixed with a binder, plasticizer, and dispersant dissolved in

https://dx.doi.org/10.1021/acsami.0c13021
ACS Appl. Mater. Interfaces 2020, 12, 46119–46131

ethanol and acetone. Thereafter, the mixtures were ball-milled to homogenize the suspensions. A wire-wound rod coater (automatic film applicator 1137, Sheen Instrument, Ltd.) was used to cast the $LiAlO_2$ green films. Detailed procedures on synthesizing green films using LF-FSP-derived NPs can be found elsewhere.[38,39] To improve packing density, the $LiAlO_2$ films were uniaxially pressed using a heated bench top press (Carve, Inc.) at 100 °C/10 kpsi/5−10 min.

Sintering studies were conducted using a high-temperature vacuum/gas tube furnace (Richmond, CA). The $Li_{1.72}AlO_2$, $Li_{1.99}AlO_2$, $Li_{3.1}AlO_2$, and $Li_{6.2}AlO_2$ green films were placed between Al_2O_3 disks and sintered at 1100 °C/2 h/air (100 mL min^{-1}).

2.3. Symmetric Cell Assembly. $Li/Li_{3.1}AlO_2/Li$ symmetric coin cells were assembled inside an Ar-filled glove box. Prior to symmetric cell assembly, the lithium metal foil (99.9%, Sigma-Aldrich) was scraped to expose a clean surface. Solid-state symmetric cells were assembled by placing the $Li_{3.1}AlO_2$ (25 μm-thick and 18 mm diameter) between the two Li foil disks. The symmetric cell was heated to 200 °C to reduce interfacial impedance. The $Li/Li_{3.1}AlO_2/Li$ cell was then transferred to the coin 2032 cell and uniaxially pressed at 0.1 kPa. The cell was cycled at ambient conditions using a potentiostat/galvanostat (BioLogic SP-300).

The analytical methods are included in the Supporting Information.

3. RESULTS AND DISCUSSION

In the present work, we first discuss the characterization of LF-FSP-produced $LiAlO_2$ NPs with various Li contents by SEM, TGA, FTIR, and XRD. In the second part, we assess the overall conductivity, phase purity, and microstructure of $Li_{1.72}AlO_2$, $Li_{1.99}AlO_2$, $Li_{3.1}AlO_2$, and $Li_{6.2}AlO_2$ membranes. In addition, the electrochemical performance of the $LiAlO_2$ membrane in a symmetric cell configuration is also presented.

3.1. Characterization of As-Produced NPs. NPs of $LiAlO_2$ with 60, 80, 150, and 300 wt % excess lithium propionates were produced by LF-FSP, as shown in Figure 1. Excess Li is used to compensate for loss during combustion and sintering. Most studies indicate that excess Li (10−15 wt. %) is required to sinter 1−2 mm-thick pellets of Li-based ceramics.[7,40]

Figure 2a shows FTIR spectra of as-produced $LiAlO_2$ NPs. The spectra show sharp peaks at 595 and 656 cm^{-1} assigned to υAl−O for octahedral Al. Bands centered near 715 and 972 cm^{-1} are ascribed to υAl−O for tetrahedral Al and symmetric bending of Al−O−H, respectively.[23,41,42] A broad peak at ~1500 cm^{-1} corresponds to carbonate υC═O.[7] The υC═O intensity increases with lithium content corresponding to increases in Li_2CO_3. The presence of Li_2CO_3 is in good agreement with TGA mass losses (~700 °C) and XRD plots, see Figures 3d and 4, respectively.

Figure 2b shows an SEM image of as-produced $Li_{6.2}AlO_2$ NPs showing spherical morphologies typical of flame-made NPs with average particle sizes (APSs) < 100 nm.[38,39] No noticeable differences in morphology were observed for $LiAlO_2$ NPs with varying Li contents, as shown in Figure S1. The particles are agglomerated (electrostatically bonded) but not aggregated (necked), which is highly desirable for facile dispersion, tape casting, and sintering dense thin films with average grain sizes (AGSs) < 10 μm. The BET N_2 adsorption-derived specific surface areas (SSAs) and APSs for the $LiAlO_2$ NPs are listed in Table 1. The spherical NPs offer a narrow size distribution with APSs of ~33−64 nm.

In Figure 3, TGA−DTA curves for $LiAlO_2$ NPs, after heating to 1000 °C/10 °C min^{-1}/air, reveal mass losses below 250 °C, ascribed to physi/chemisorbed water on the as-produced NP surfaces. As the Li content increases to 300 wt %, the TGA plot shows an endotherm associated with a mass loss starting at ~700 °C as Li_2CO_3 melts/decomposes with loss of CO_2 ending at ~900 °C.[7] The slightly higher mass losses for $Li_{6.2}AlO_2$ suggest a hygroscopic nature coincident with a higher propensity to pick up CO_2 as might be expected with the higher Li content. This mass loss behavior is further confirmed by XRD (Figure 4) data indicating the presence of Li_2CO_3.

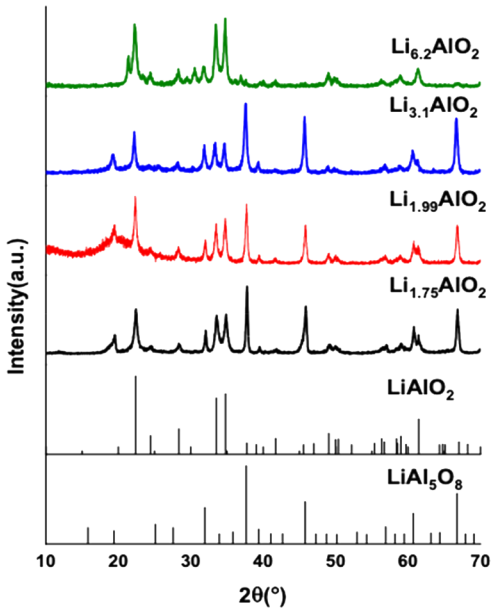

Figure 4. XRD plots of as-produced $LiAlO_2$ NPs.

Table 1. SSAs and APSs of $LiAlO_2$ NPs

NPs	SSAs (m^2 g^{-1})	APSs (nm)
$Li_{1.75}AlO_2$	53	33
$Li_{1.99}AlO_2$	46	40
$Li_{3.1}AlO_2$	43	47
$Li_{6.2}AlO_2$	38	64

The crystal structures of lithium aluminate polymorphs have been studied since the 60s[43] based on the $A^{+1}B^{+3}O_2$ formula by powder neutron and single-crystal X-ray techniques.[44] Polymorphs of lithium aluminum oxides with six different crystal systems have been identified to date.[45] As might be expected, phase formation depends on the processing conditions used. Here, we only focus on cubic $LiAl_5O_8$ and γ-$LiAlO_2$ phases.

Figure 4 shows XRD plots of as-produced $LiAlO_2$ NPs with varying Li amounts. The primary phase is $LiAlO_2$ with a secondary Al-rich $LiAl_5O_8$ phase. Table 2 shows the wt % fraction of each phase. The combustion byproducts H_2O and CO_2 at high flame temperatures (>1000 °C) accelerate decomposition; hence, the formation of single-phase $LiAlO_2$ was inhibited even with 300 wt % excess Li. In general, LF-FSP-made NPs are pure oxides.[38,46] However, here, we obtain

Table 2. Relative Contents of Phases in As-Produced $LiAlO_2$ NPs

NPs	$LiAlO_2$ (wt %)	$LiAl_5O_8$ (wt %)	Li_2CO_3 (wt %)
$Li_{1.75}AlO_2$	25 ± 0.2	74 ± 0.8	
$Li_{1.99}AlO_2$	42 ± 0.5	57 ± 0.5	
$Li_{3.1}AlO_2$	67 ± 0.2	32 ± 0.8	
$Li_{6.2}AlO_2$	85 ± 0.4	5 ± 0.2	9.6 ± 0.6

https://dx.doi.org/10.1021/acsami.0c13021
ACS Appl. Mater. Interfaces 2020, 12, 46119−46131

a mixture of $LiAl_5O_8$, Li_2CO_3, and $LiAlO_2$. Owing to combustion followed by rapid quenching, LF-FSP-produced NPs often exhibit kinetic rather than thermodynamically favored phases; consequently, as-produced NPs are often mixed phases.[7,39,47] The XRD plots show broad peaks ~19° 2θ, suggesting the amorphous nature of the as-produced powders. It is typical for LF-FSP-derived electrolyte-targeted NPs to be at least partially amorphous as a result of the fast combustion and quenching process.[9,38]

The observed broad diffraction peaks for the as-produced NPs is due to the combined effect of the microstrain induced by dislocation (strain broadening) and shrinkage of coherent scattering volume (size broadening).[48] Williamson−Hall (W−H)[49] analysis was used to calculate the crystallite size (β_s) and microstrain (β_e) by considering the broadening of the peak width as a function of 2θ. The total broadening can be expressed as

$$\beta_t = \beta_s + \beta_e \quad (1)$$

where β_t represents the total broadening, β_s is the broadening due to the crystallite size, and β_e is due to the microstrain. It is well known that the Scherrer formula provides the APSs of crystallites in a direction perpendicular to particular (hkl) planes.[50] Thus, the $LiAlO_2$ NP crystallite sizes are estimated using the Scherrer formula (eq 2)

$$D = k\lambda/\beta_s \cos\theta \quad (2)$$

where D is the crystallite size, $k = 0.94$ is the shape factor, λ is the X-ray wavelength (0.154 nm), β_s is the full width at half-maximum (FWHM) in radians, and θ is the diffraction angle of Bragg. The XRD peak broadening due to the microstrain is given by eq 3

$$\beta_e = 4\varepsilon \tan\theta \quad (3)$$

The W−H method assumes that the strain is uniform throughout the crystallographic direction, given by introducing eqs 2 and 3 into eq 1

$$\beta_t \cos\theta = k\lambda/D + 4\varepsilon \sin\theta \quad (4)$$

In eq 4, D and ε correspond to the crystallite size and microstrain, respectively. Figure S2 shows the W−H plots for the as-produced $LiAlO_2$ NPs. The nonlinearity in the W−H plot (Figure S2b) indicates the presence of the anisotropic strain.[51] The gradient of $\beta_t \cos\theta$ versus $\sin\theta$ plot gives the NP microstrain, and the Y-axis intercept gives the $k\lambda/D$ value.

Table S3 lists the estimated average values for the crystallite size and microstrain based on W−H plots. The reported BET APSs (Table 1) are relatively larger than the XRD crystallite size. The variation between these measurements indicates that the NPs are agglomerated,[52] in good agreement with the NP microstructures shown by the SEM image in Figure 2b. Although the Scherrer formula provides only a lower limit of crystallite size, both BET APSs and XRD crystallite sizes increase linearly with excess Li for the as-produced $LiAlO_2$ NPs, as shown in Figure 5.

Figure 6a,b shows ^{7}Li and ^{27}Al MAS NMR spectra of $Li_{6.2}AlO_2$ NPs, respectively. The ^{7}Li MAS NMR spectrum shows a single peak at 0.3 ppm consistent with the crystal structure of $LiAlO_2$ that contains only a single Li site with tetrahedral oxygen coordination. The ^{27}Al MAS NMR spectrum shows two peaks. The first, at 76.2 ppm, is characteristic of $[AlO_4]$ units,[53,54] as expected from the crystal

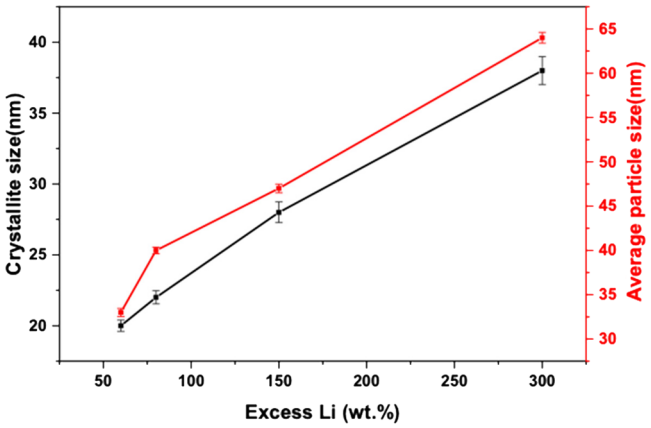

Figure 5. Comparison of BET APSs and XRD crystallite sizes.

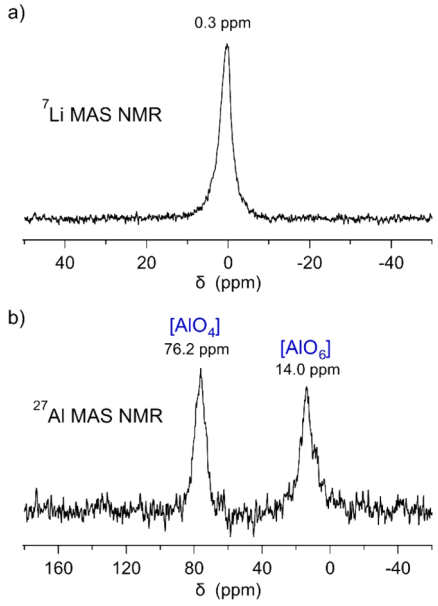

Figure 6. (a) ^{7}Li and (b) ^{27}Al MAS NMR spectra of $LiAlO_2$ NPs.

structure of $LiAlO_2$. The second peak at 14.0 ppm clearly shows the presence of $[AlO_6]$ units.[53,54] This might hint at the presence of some residual $LiAl_5O_8$ where Al is present both on tetrahedral and octahedral sites of the spinel structure, supporting the XRD results present in Figure 4. Furthermore, since both peaks are quite broad, some amorphous fractions might be present in the sample.

The crystal structure of $LiAl_5O_8$ (Figure 7) shows corner-linked Al−O forming tetrahedra and edge-shared Li/Al−O octahedra. The four Li ions in the unit cells labeled Li1, Li2, Li3, and Li4 are distributed on octahedral sites.[55] Meanwhile, Al^{3+} is equally distributed between tetrahedral and octahedral sites. $LiAl_5O_8$, owing to its high symmetry, has four equivalent Li^+ sites with the same diffusion path(s).[55] Hence, it has been suggested that $LiAl_5O_8$ might show high ionic conductivities.[55] Table S4 lists the lattice parameters for $LiAl_5O_8$ obtained from experimental data and theoretical modeling.

As mentioned above, the large interfacial resistivity between the metallic Li anode and garnet-type $Li_7La_{2.75}Ca_{0.25}Zr_{1.75}Nb_{0.25}O_{12}$ (LLCZN) was effectively decreased by introduction of an ultrathin alumina coating.[12] The rationale for these observations suggests formation of a lithiated alumina that permits rapid diffusion of Li^+ through the

https://dx.doi.org/10.1021/acsami.0c13021
ACS Appl. Mater. Interfaces 2020, 12, 46119−46131

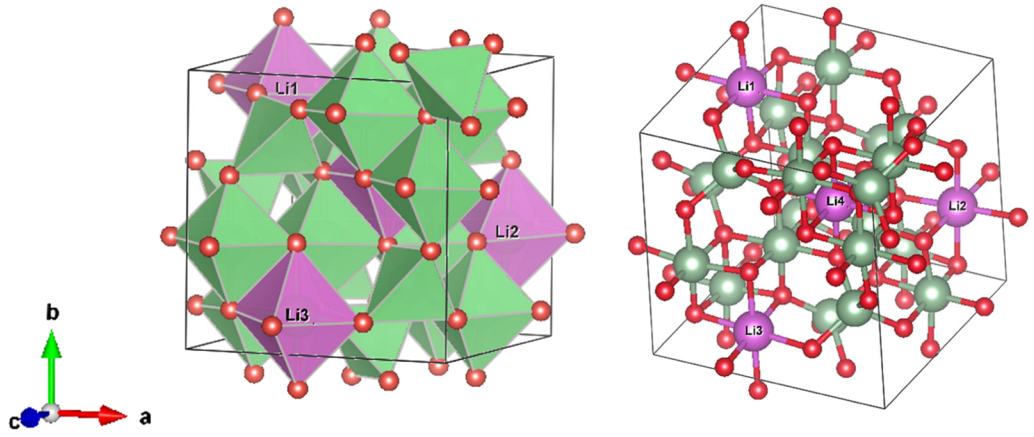

Figure 7. Crystal structures of $LiAl_5O_8$. The Li, Al, and O are shown in pink, green, and red, respectively; unit cell in black.

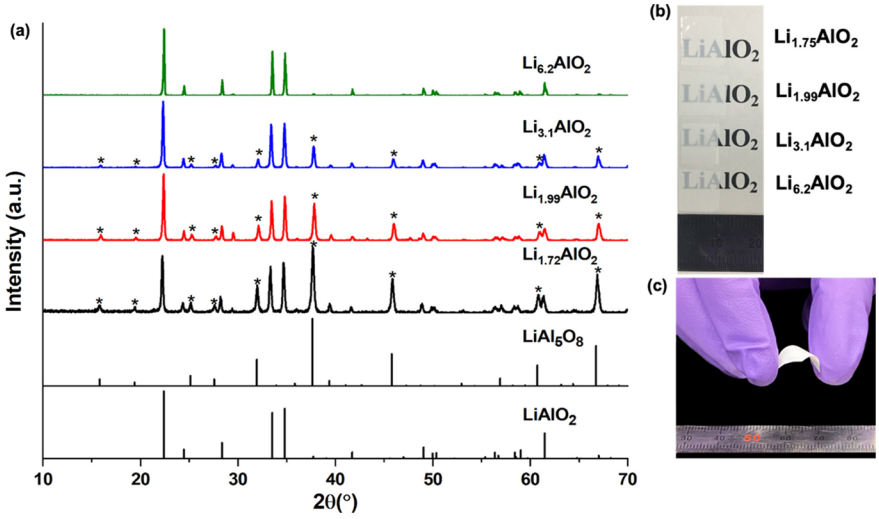

Figure 8. (a) XRD patterns of sintered $LiAlO_2$ membranes (1100 °C/2 h/air). (b, c) Optical images of (b) translucent $LiAlO_2$ membranes and (c) flexible $Li_{3.1}AlO_2$ film. (The asterisk symbol corresponds to $LiAl_5O_8$.)

interface.[12] One implication is that the $LiAl_5O_8$ framework may permit high Li^+ mobility via 3D diffusion.[55]

Pan et al.[55] studied Li^+ diffusion mechanisms in $LiAl_5O_8$ and alumina by first-principles density functional theory (DFT) calculations. They find that the Li^+ diffusion coefficient for $LiAl_5O_8$ ($D_{Li^+} = 3.6 \times 10^{-8}$ cm^2 s^{-1}) is significantly higher than that of alumina ($D_{Li^+} = 9.3 \times 10^{-48}$ cm^2 s^{-1}) at room temperature, suggesting that the mobility of Li^+ in $LiAl_5O_8$ is substantially improved. Therefore, enhanced interfacial impedance may be accessed by replacing alumina coatings with $LiAl_5O_8$, implying better battery performance. In addition, $LiAl_5O_8$ shows a wide electrochemical stability window of 0.8−4.08 V versus Li/Li^+, making it an attractive coating for next-generation LIB electrodes[55] and a potential solid electrolyte for assembling microbatteries.

3.2. Microstructure and Crystallinity of $LiAlO_2$ Membranes. Multiple studies have used conventional solid-state synthesis methods to produce $LiAlO_2$ powders.[41] However, this technique often produces aggregated materials with broad particle size distributions, low SSAs, and requiring multiple process steps to fabricate dense, single-phase, and thick films.[38] In contrast, we have reported using flame-made NPs with narrow APSs to directly process green films by ball milling the NPs with polymer additives followed by conventional tape casting. Thermopressing the green films at 100 °C/10 kpsi/10 min results in uniform green body density that can drive densification at lower sintering temperatures with control of final grain size and good mechanical properties in thin (<50 μm) films.

Prior to sintering, solid loadings were confirmed by TGA (Figure S3), presenting an expected ceramic yield of 70 wt % matching theory. The mass loss between 200 and 400 °C is ascribed to decomposition of the polymeric additives. This step is necessary to establish gentle binder burnout temperatures (300 °C/2 h) to avoid cracking the polymer-free films. Green films of $LiAlO_2$ with varying Li amounts were subsequently sintered at various densification temperatures. Figure S4 shows SEM images of the green films. Microstructures demonstrate that the NPs are well mixed with the polyacrylic acid dispersant. Green films of $LiAlO_2$ were inserted between α-Al_2O_3 disks and debindered at 300 °C/2 h and 665 °C/2 h/5 °C min^{-1} followed by sintering at 1100 °C/2 h/1 °C min^{-1} under a 120 mL min^{-1} air flow.

Figure 8a shows XRD patterns of $LiAlO_2$ membranes sintered at 1100 °C/2 h/air. The dwell time was minimized to 2 h, to reduce Li volatility, preferably resulting in a single-phase, dense $LiAlO_2$. $LiAlO_2$ membranes with 60, 80, and 150 wt % excess Li showed the targeted γ-$LiAlO_2$ and $LiAl_5O_8$.

https://dx.doi.org/10.1021/acsami.0c13021
ACS Appl. Mater. Interfaces 2020, 12, 46119−46131

Table 3 shows the relative wt % fraction of the phases present. For Rietveld refinement, a model was imported from the

Table 3. Weight Fraction of Phases in $LiAlO_2$ Thin Films Sintered at 1100 °C/2 h/Air

thin films	$LiAlO_2$ (wt %)	$LiAl_5O_8$ (wt %)
$Li_{1.75}AlO_2$	35 ± 0.6	64 ± 0.4
$Li_{1.99}AlO_2$	53 ± 0.8	46 ± 0.2
$Li_{3.1}AlO_2$	72 ± 0.8	27 ± 0.2
$Li_{6.2}AlO_2$	100	

Inorganic Crystal Structure Database (ICSD), $LiAlO_2$ (PDF-01-095-3721) and $LiAl_5O_8$ (PDF-04-022-2622). $Li_{6.2}AlO_2$ membranes show single-phase $LiAlO_2$ (space group, $P4_12_12$), indicating that loss of Li is compensated by using excess lithium propionate. Hence, the LF-FSP synthesis method allows exceptional control of phase purity and stoichiometry.

It is common to account for the loss of Li in sputtering techniques to synthesize phase pure γ-$LiAlO_2$.[45] However, such processing requires subsequent ball milling of raw materials followed by compacting pellets and sintering at high temperatures (~1100 °C) and long dwell times (20 h) to produce dense targets.[45]

Marezio[43] reported that the *XZ* plane of γ-$LiAlO_2$ consists of distorted MO_4 tetrahedra (M = Li and Al), forming a 3D network. The unit cell contains four formula units. One edge of the tetrahedron is shared by other tetrahedra containing a metal ion of a different kind.

As seen in Figure 9, the edge-sharing topology generates distorted hexagonal channels. In this study, the experimental *c*/*a* ratio (1.212) for the $Li_{6.2}AlO_2$ membrane is consistent with that reported in literature studies (within 1% error).[45,56] The calculated average Li−O distance in the tetrahedral structure is ~2 Å, also in good agreement with the theoretical modeling work.[56] To locate the equilibrium structure, the unit cell parameters and atomic coordinates were fully relaxed. The lattice parameters for $LiAlO_2$ obtained from experimental and theoretical calculations are listed in Table S5.

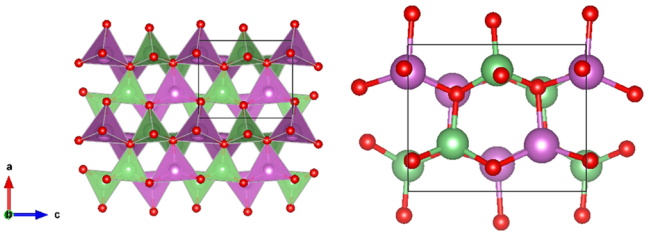

Figure 9. Crystal structure of $LiAlO_2$. The Li, Al, and O are shown in pink, green, and red, respectively; unit cell in black.

Figures 8b and 10 show optical images and SEM fracture surfaces of $LiAlO_2$ membranes with various Li contents sintered at 1100 °C/2 h/air, respectively. The optical images with dimensions of ~1 × 1 cm^2 reveal semitransparent, sintered membranes. Translucency arises because of high densities.[39] The $Li_{1.72}AlO_2$ membrane, with the highest $LiAl_5O_8$ phase fraction (64.4 wt %), exhibits a glossy surface (Figure 8b). The dense membranes offer thicknesses of 20−50 μm. SEM fracture surface images show uniform submicrometer-sized pores, ascribed to the small and uniform NP APSs, as shown in Figure 2b and Figure S5. This is significant because macroscopic pores (>10 μm) in ceramic electrolytes, aside from engendering poor mechanical properties, result in poor ionic conductivity from local inhomogeneous ion mobility, decreasing battery cycle life.[57]

Figure 8c shows that the $Li_{3.1}AlO_2$ thin membrane offers mechanical properties that allow it to flex, which can be expected to permit roll-to-roll processing and facilitate assembly of microbatteries. This flexible electrolyte membrane also enables fabrication of new ASSB battery designs. In general, fine-grained membranes ensure flexibility in ceramics attributed to the tortuous crack propagation pathways, resulting in superior mechanical stability. The flexibility of the membrane also indicates the absence of surface flaws that may initiate cracking.

In general, high-density microstructures were achieved at low sintering temperatures for all $LiAlO_2$ films. Transgranular fracture surfaces reveal very high densities. The density of the membranes seems to increase as excess Li increases as the $Li_{6.2}AlO_2$ membrane shows the highest relative densities ~95 ± 0.2% as determined by the Archimedes method (Table 4). This may also be attributed to the fact that as-produced $Li_{6.2}AlO_2$ NPs contain excess Li_2CO_3, which aids in liquid phase/reaction driven sintering as seen previously.[47] The AGSs for the $LiAlO_2$ films were calculated by the linear intercept method.[58] Table 4 shows that AGSs increased from 2.2 ± 0.3 μm (for $Li_{1.72}AlO_2$) to 7.2 ± 0.5 μm (for $Li_{6.2}AlO_2$) with increasing γ-$LiAlO_2$ phase. The small AGSs for $Li_{1.72}AlO_2$ (Figure S5) and $Li_{1.99}AlO_2$ translate to increases in grain boundary volume fractions, which will reduce the relative densities for these membranes. Thus, the found densities reported may actually be somewhat higher because the exact volume fraction and densities of the grain boundaries are not known.

3.3. Ionic Conduction Mechanisms in $LiAlO_2$/$LiAl_5O_8$ Membranes. $LiAlO_2$ is a known electrical insulator and a very poor Li^+ conductor (~10^{-10} S cm^{-1}) at room temperature.[45] Efforts have been made to improve its ionic conductivity by introducing an amorphous phase,[6] silicate-based Li^+ conducting components with higher ionic conductivity,[59] structural disordering via point defects, and higher dimensional defects.[37] However, significant improvements in ionic conductivity have not been reported, to the best of our knowledge. In this work, we examined the effect of a secondary phase, $LiAl_5O_8$, on $LiAlO_2$ membrane conductivity. Figure 11 shows typical Nyquist plots for the $LiAlO_2$ membranes where electrochemical impedance was collected from 7 MHz to 1 Hz at 25 °C. The Nyquist plots in the temperature range of −10 to 100 ° C are presented in Figures S6 and S7. The $Li_{3.1}AlO_2$ + 150% membranes offer the highest ionic conductivity of ~5.2 ± 0.7 × 10^{-6} S cm^{-1} at room temperature. Table S6 records total ionic conductivities of the membranes heated to selected temperatures.

Optimization of the ionic conductivity of γ-$LiAlO_2$ was achieved by introducing $LiAl_5O_8$. Pristine γ-$LiAlO_2$ membranes show room-temperature conductivities of 2.4 ± 1.2 × 10^{-8} S cm^{-1}, still 2 orders of magnitude higher than typically reported for γ-$LiAlO_2$.[6] For conventional all-solid-state microbatteries, thin-film electrolytes with ambient conductivities >10^{-6} S cm^{-1} are highly desirable.[36,60] Hence, these new $LiAlO_2$/$LiAl_5O_8$ membranes are solid electrolyte alternatives to LiPON for assembly of microbatteries.

The Li^+ migration pathways in $LiAlO_2$/$LiAl_5O_8$ mixed phases are proposed to be shorter than the distance between nearest Li^+ sites in pristine γ-$LiAlO_2$, which implies occupation

https://dx.doi.org/10.1021/acsami.0c13021
ACS Appl. Mater. Interfaces 2020, 12, 46119−46131

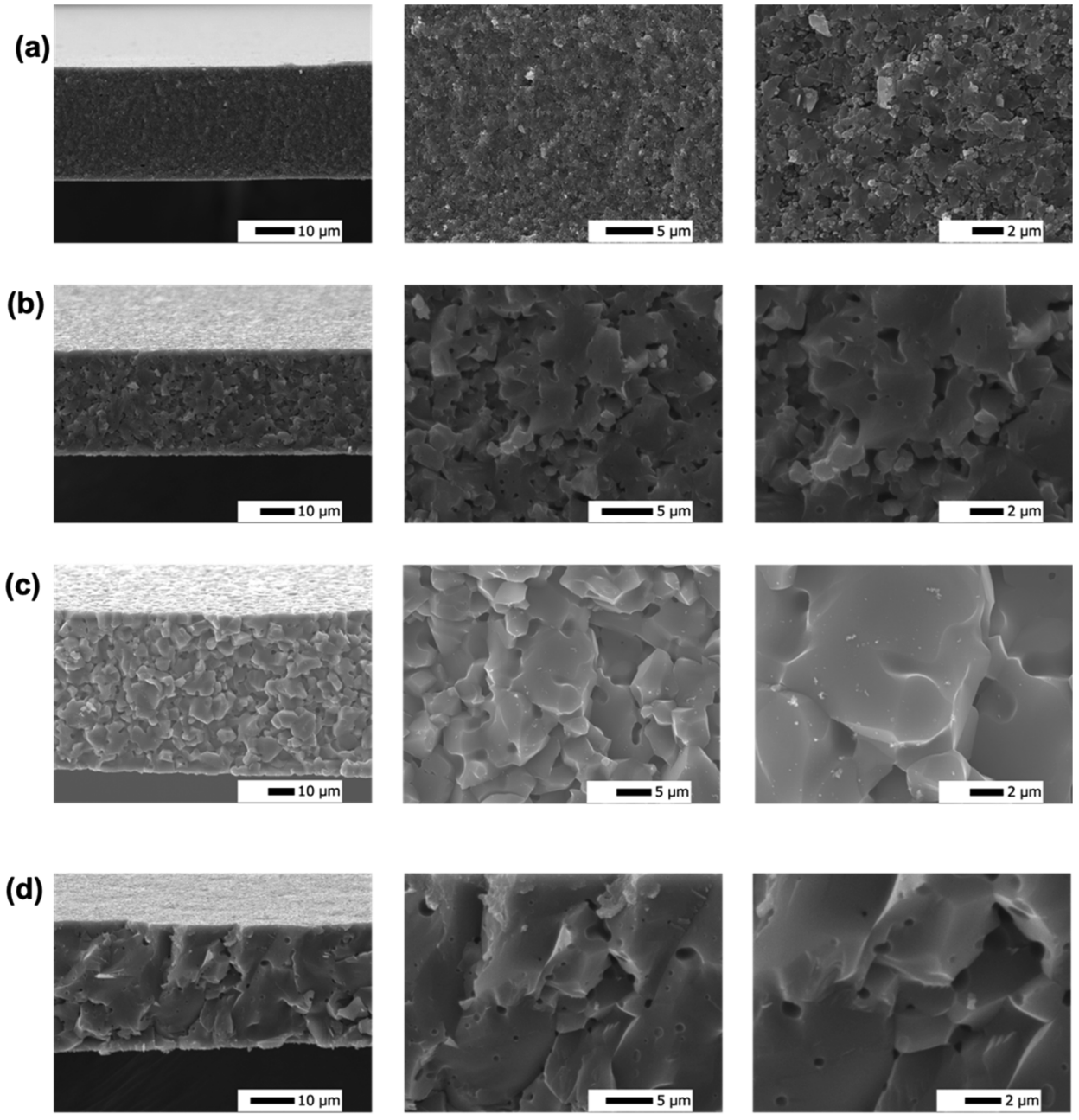

Figure 10. (a–d) SEM fracture surface images of $LiAlO_2$ membranes sintered at 1100 °C/2 h. (a) $Li_{1.75}AlO_2$, (b) $Li_{1.99}AlO_2$, (c) $Li_{3.1}AlO_2$, and (d) $Li_{6.2}AlO_2$.

Table 4. Relative Densities of $LiAlO_2$ Thin Films Sintered at 1100 °C/2 h/Air

thin films	density (%)	AGSs (μm)
$Li_{1.75}AlO_2$	83 ± 0.2	2.2 ± 0.3
$Li_{1.99}AlO_2$	87 ± 0.5	4.5 ± 0.7
$Li_{3.1}AlO_2$	90 ± 0.6	6.6 ± 0.2
$Li_{6.2}AlO_2$	95 ± 0.2	7.2 ± 0.5

of interstitial sites with lower activation energies. $LiAl_5O_8$ ionic conductivity originates from diffusion of point defects (V_{Li}^- and Li_i^+).[55] The Li^+ interstitial diffusion pathway has been reported to show a substantial decrease in the interstitial migration barrier (0.33 eV) compared to Li^+ vacancy diffusion.[55]

This is ascribed to a direct hopping mechanism where interstitial Li^+ diffuses through the shared edge between two LiO_4 tetrahedra (Figure 7), resulting in comparatively shorter Li–O bonds (~1.4 Å).[55] Meanwhile, the vacancy migration activation energy is reported to be as high as 2.86 eV due to electrostatic repulsion from adjacent Al^{3+} at the midpoint between the two Li vacant sites.[55]

Wiedemann et al.[45] showed that Li^+ diffusion in $LiAlO_2$ occurs along a strongly curved pathway in 2D via hopping of Li^+ between Li positions and adjacent vacancies. The reported migration barrier for this diffusion mechanism is ~0.72 eV, which was determined using temperature-dependent neutron diffraction studies. The other diffusion mechanism reported is through a long-range diffusion along the [001] direction, which results in a higher activation energy of 0.87 eV.[45] Indris et al.[61]

https://dx.doi.org/10.1021/acsami.0c13021
ACS Appl. Mater. Interfaces 2020, 12, 46119–46131

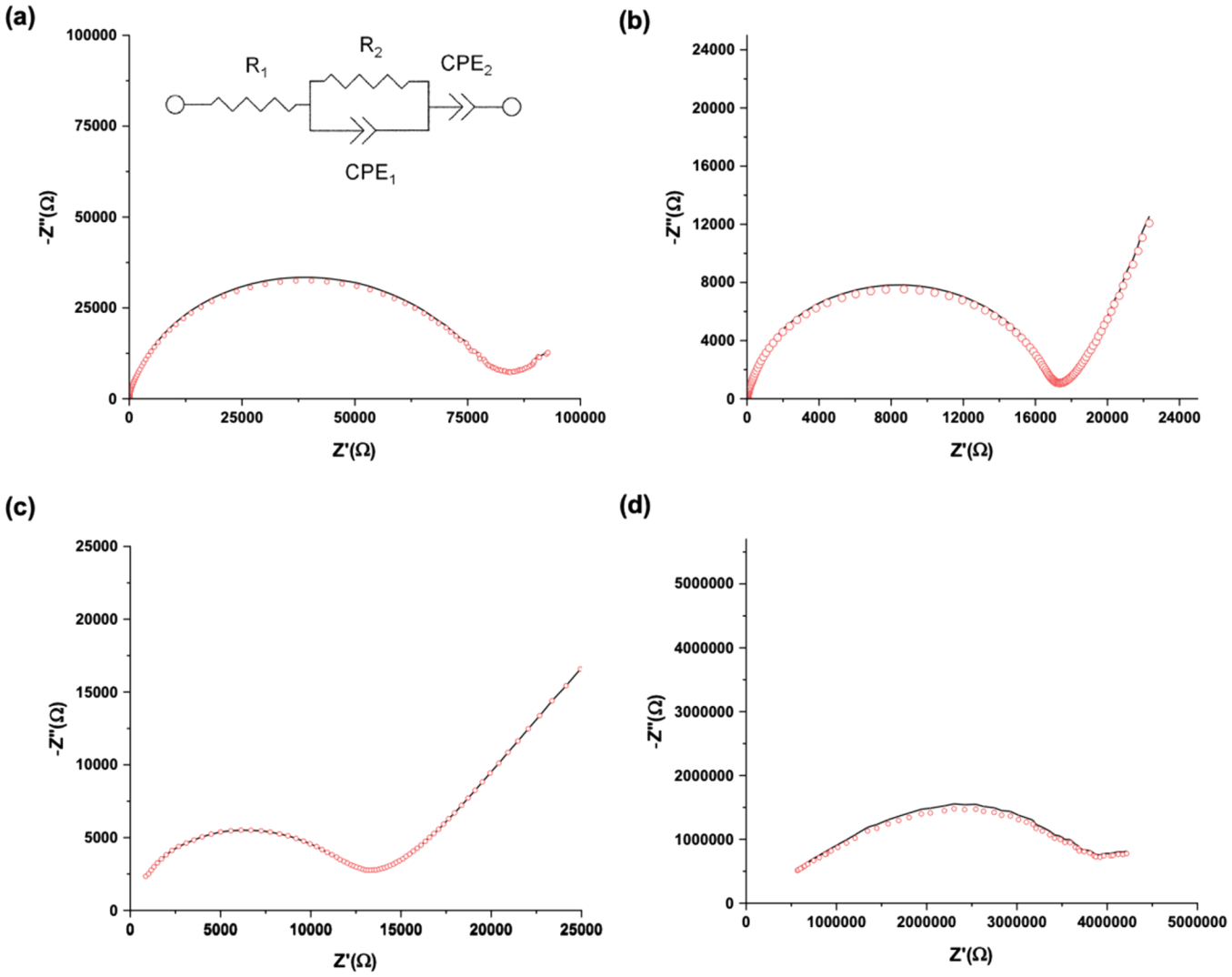

Figure 11. (a–d) Nyquist plots of (a) $Li_{1.72}AlO_2$, (b) $Li_{1.99}AlO_2$, (c) $Li_{3.1}AlO_2$, and (d) $Li_{6.2}AlO_2$ membranes at 25 °C. Marked lines indicate the equivalent circuit modeling data, and the circles represent experimental data.

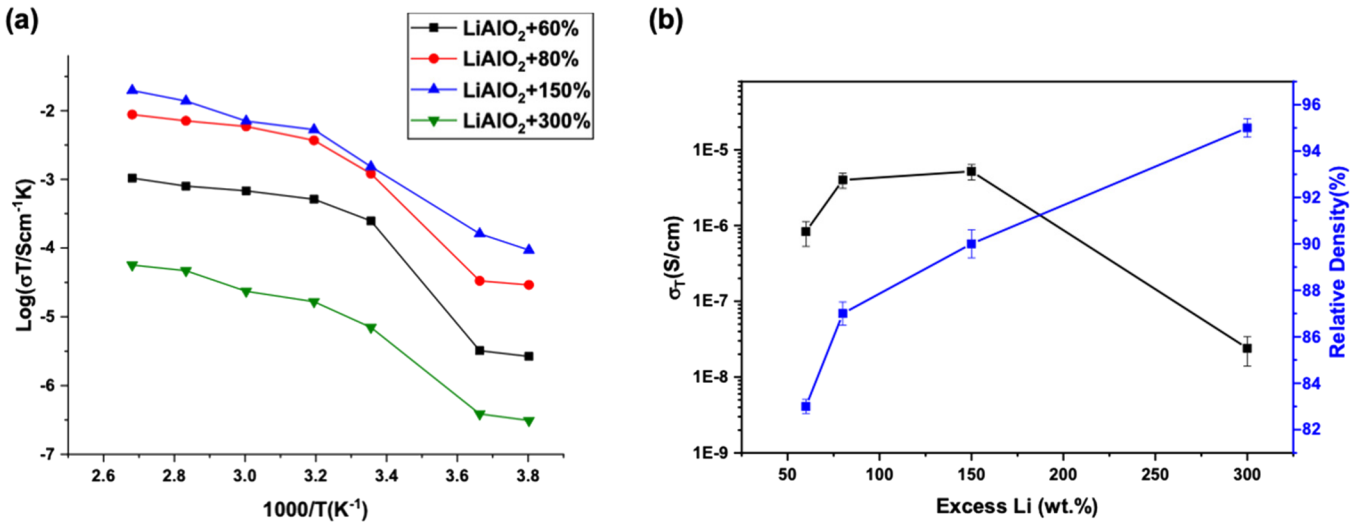

Figure 12. (a) Arrhenius plots for the ionic conductivity. (b) Relation between room-temperature ionic conductivities and relative densities of $LiAlO_2$ membranes sintered at 1100 °C/2 h.

investigated Li^+ diffusion in $LiAlO_2$ single crystals by ^7Li NMR spectroscopy and conductivity measurements. They reported a barrier activation energy of 0.72 eV ascribed to the Li^+ diffusion via a vacancy mechanism.[61]

https://dx.doi.org/10.1021/acsami.0c13021
ACS Appl. Mater. Interfaces 2020, 12, 46119–46131

Table 5. Comparison of Conductivities of $LiAlO_2$ Samples with Various Processing Methods[a]

processing	phase composition	experimental conditions	σ (S cm^{-1})	thickness	ref
LF-FSP/TC	γ-$LiAlO_2$ (~73 wt %)/$LiAl_5O_8$ (~27 wt %)	AC impedance: rt	5.2×10^{-6}	25 μm	this work
ALD	amorphous Li/Al = 1:1.16	impedance: in-plane	5.1×10^{-9}	90 nm	6
ALD	amorphous $LiAlO_2$	impedance: in-plane	5.6×10^{-8}	50 nm	16
ALD	amorphous $LiAlO_2$	impedance: cross-plane	2.8×10^{-10}	160 nm	6
CT	single-crystalline γ-$LiAlO_2$	AC impedance: 150−350 °C	1×10^{-17}	80 mm	61
SSR	polycrystalline γ-$LiAlO_2$	AC impedance: 450−1000 °C	2×10^{-14}	2.9 mm	59
TRQ	$0.7Li_2O/0.3Al_2O_3$	AC impedance: 150−400 °C	5×10^{-8}	20 μm	63

[a]TRQ = twin roller quenching, SSR = solid-state reaction, TC = tape casting, CT = Czochralski technique, ALD = atomic layer deposition, and LF-FSP = liquid-feed flame spray pyrolysis.

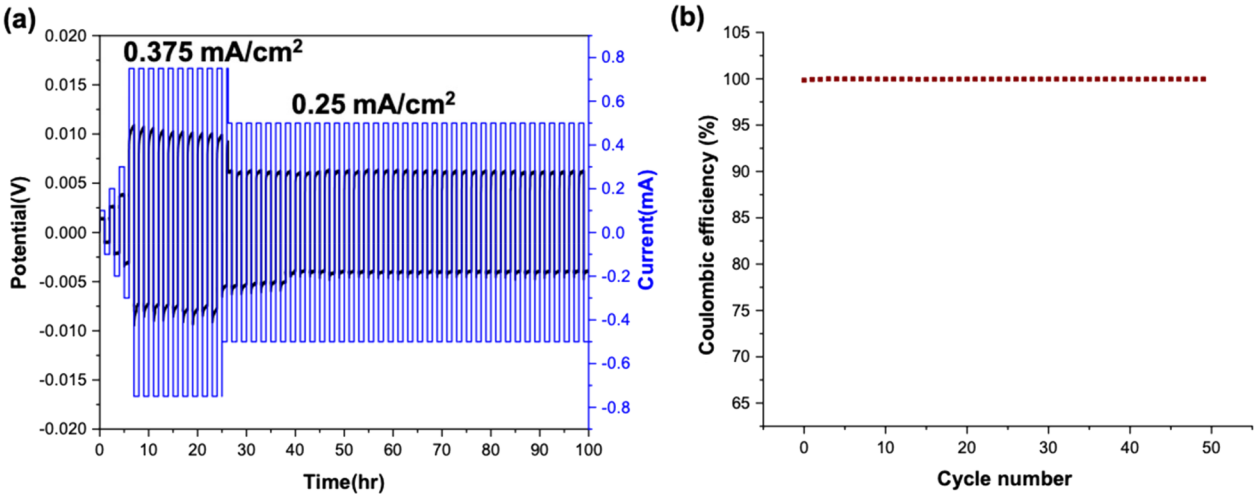

Figure 13. Galvanostatic cycling of the Li/$Li_{3.1}AlO_2$/Li cell at ambient using various current densities of 0.05−0.375 mA cm^{-2}. (a) Voltage vs time profile and (b) Coulombic efficiency vs cycle number plot of the symmetric cell.

The introduction of structural disorder caused by point defects and higher-dimensional defects in γ-$LiAlO_2$ has been reported to increase the room-temperature ionic conductivity, experimentally studied by temperature-dependent impedance spectroscopy.[37] A recent study elucidates the local diffusion mechanism for γ-$LiAlO_2$ by a climbing image nudged elastic band approach with periodic quantum mechanical density functional theory.[56]

It was concluded that Li^+ can diffuse between two LiO_4 tetrahedral sites (Figure 9) via Li point defects (V_{Li}^-) and via a Li^+ Frenkel defect (V_{Li}^- and Li_i^+).[56] The low activation barriers reported here are ascribed to the presence of extrinsic defects generated by the introduction of $LiAl_5O_8$. The Arrhenius plots for the ionic conductivity of $LiAlO_2$ membranes are shown in Figure 12a. The conductivity of the $LiAlO_2$ membranes increases with increasing temperature, indicating a thermally activated mechanism. Table S7 presents activation energies ranging from 0.43 to 0.5 eV for $LiAlO_2$ membranes with various Li compositions.

The ionic conduction mechanism for γ-$LiAlO_2$ is disparate with activation barriers ranging from 0.5 to 1.47 eV.[45,61,62] These findings are based on polycrystalline, microcrystalline, single-crystalline, and nanocrystalline γ-$LiAlO_2$.[45,56,61,62] The discrepancies in the calculated activation energies might be ascribed to the fact that only isolated vacancies are considered as possible defects, disregarding contributions from grain boundaries and complex morphologies. In addition, Frenkel defect-type Li^+ migration involves local Li^+ jumps as a function of V_{Li}^- and the distance between migrating Li−Li_i^+, which explains the relatively large scatter in the experimental activation energy values.[56]

Figure 12b shows the relationship between room-temperature ionic conductivities and relative densities of $LiAlO_2$ membranes with various Li amounts sintered at 1100 °C/2 h. The single-phase γ-$LiAlO_2$ film, with a high relative density of ~95%, shows 2 orders of magnitude lower ionic conductivity (2.4×10^{-8} S cm^{-1}) compared to the mixed-phase $LiAlO_2/LiAl_5O_8$ films, with slightly lower densities. The presence of the $LiAl_5O_8$ phase results in superior Li^+ diffusivity (3.6×10^{-8} cm^2 s^{-1}) and lower migration barriers.[55] Moreover, the fine-grained membranes (AGSs < 5 μm) ensure that cracks propagate through a tortuous path that absorbs the energy driving propagation, offering superior mechanical stability.

Table 5 lists the thicknesses, processing methods, and ambient ionic conductivities of various $LiAlO_2$ films/pellets reported in literature. The gas-phase deposition techniques (i.e., ALD) generally require an expensive and energy-intensive process. Regardless the simplicity of the SSR method, achieving a dense, single-phase γ-$LiAlO_2$ sample requires high sintering temperatures and long dwell times. Utility for cost-effective mass production with fast ion conducting properties for ASSBs using this approach seems problematic at best.

3.4. Symmetric Cell Studies of Li/$Li_{3.1}AlO_2$/Li. Li/$Li_{3.1}AlO_2$/Li symmetric cell was cycled at ambient conditions by a DC steady-state method in which various current densities (0.05−0.375 mA cm^{-2}) were used. Figure 13a demonstrates the potential response of the Li/$Li_{3.1}AlO_2$/Li symmetric cell. At relatively low current densities (0.05−0.15 mA cm^{-2}), the

https://dx.doi.org/10.1021/acsami.0c13021
ACS Appl. Mater. Interfaces 2020, 12, 46119−46131

symmetric cell exhibits an ideal voltage response, indicating that there is a minimal interfacial impedance at ambient conditions. The $Li_{3.1}AlO_2$ membrane wets well with the Li metal (Figure S8), supporting the first-principles computational studies that demonstrate the strong chemical binding between the Li metal and $Li_xAl_2O_{3+x/2}$ (x = 0.4−1.4).[12]

The voltage plateaus during cycling at higher current density (0.375 mA cm^{-2}) do show polarization that follows Ohmic behavior. This polarization is consistent across all cycles, as shown in Figure S8, which does not suggest degradation of the $LiAlO_2$ membrane. Typically, solid electrolyte degradation is indicated by the reduction of the voltage during galvanostatic cycling. Long-term cycling at a 0.25 mA cm^{-2} current density shows that the potential profile becomes constant (∼6.5 mV) for 60 h, confirming that the lithiated $Li_{3.1}AlO_2$ membrane is a good Li^+-ion conductor that provides an effective Li^+ migration path.

The Coulombic efficiency is ∼100% (Figure 13b), suggesting that the primary charge carrier through $Li_{3.1}AlO_2$ was Li^+ with negligible electronic conductivity. This is also supported by the obtained electronic conductivity determined by DC polarization experiments. The electronic conductivities were calculated following the procedure described elsewhere.[64,65] Figure S9 shows that the stabilized current increases linearly with the step increase voltage as expected from Ohm's law. The $Li_{3.1}AlO_2$ membrane showed an average electrical conductivity of $6.7 \pm 0.4 \times 10^{-10}$ S cm^{-1}. The lithium transference number (t_{Li^+}) was calculated using eq 5

$$t_{Li^+} = (\sigma_{Li^+})/(\sigma_{Li^+} + \sigma_{e^-}) \quad (5)$$

where σ_{Li^+} is the ionic conductivity of the $Li_{3.1}AlO_2$ membrane obtained from the Nyquist plot and σ_{e^-} is the electrical conductivity deduced from the DC polarization experiments. The $Li_{3.1}AlO_2$ membrane exhibits a high lithium transference number of ∼1, enabling the mitigation of electrode concentration polarization.

3.5. $LiAlO_2$ NP-Coated $Li_4Ti_5O_{12}$(LTO) Electrode. Additional benefit of the $LiAlO_2$ solid electrolyte is that it can be used as a coating material for LIB electrodes. Even though LTO demonstrates excellent structural stability, it suffers from poor conductivity, which limits its application for high-energy density Li^+ batteries. The very low electronic conductivities (<10^{-13} S cm^{-1}) and the sluggish Li^+ diffusion coefficient of LTO result in its poor capability. It has been demonstrated that the rate capability of LTO can be improved by doping aliovalent ions,[66] reducing particle size, and incorporating conductive additives.[67] Thus, the LTO powders were coated with $LiAlO_2$ NPs to enhance the conductivity and rate performance. Prior to electrode synthesis, the LTO powder, carbon black (C65), and the $LiAlO_2$ NPs were heated to 60 °C/24 h/vacuum. The electrode slurry was prepared by mixing LTO (80 wt %), carbon black (C65, 5 wt %), $LiAlO_2$ NPs (5 wt %), and polyvinylidene difluoride (PVDF,10 wt %) in 1-methyl-pyrrolidin-2-one. The slurry was then coated on Cu foil. Figure S10 shows SEM fracture surface and EDX map images of the $LiAlO_2$-coated LTO electrode. The EDX map shows well distributed (Al, C, F, Ti, and O) ascribed to the $LiAlO_2$ electrolyte, carbon additive, PVDF binder, and LTO powder. The top interface is mainly composed of Cu from the current collector. Here, we demonstrate that it is possible to introduce $LiAlO_2$ coatings onto electrodes by simple ball milling and tape casting methods.

Furthermore, the tape casting process permits stacking of these $LiAlO_2/LiAl_5O_8$ green films onto electrodes, which simplifies battery design. Figure S11 shows the SEM and EDX fracture surface images of LTO/$LiAlO_2$ membranes. The SEM fracture surface image shows that the interface between the anode and the electrolyte is smooth and uniform. The thicknesses of LTO and $LiAlO_2$ are ∼45 and 25 μm, respectively. The EDX map shows well distribution of Al in the top layer and Ti in the bottom layer ascribed to $LiAlO_2$ and LTO, respectively. The O and C elements are also well distributed throughout the anolyte electrode. This preliminary work demonstrates that the $LiAlO_2$ membranes have a potential to be assembled in ASSBs. The electrochemical performance of the $LiAlO_2$-coated LTO electrode is beyond the scope of this paper.

4. CONCLUSIONS

Solid electrolytes are proposed as key components in developing next-generation ASSBs due to their unique merits in terms of wide operating voltage, high thermal and mechanical stability, and safety. The LF-FSP method's facility in the fabrication of nanoparticles with spherical morphologies enables low-temperature sintering that limits grain growth during densification, leading to dense $LiAlO_2$ membranes that are thermally and chemically stable and therefore of use as coatings and electrolytes for next-generation LIBs. The new composite $LiAl_5O_8/LiAlO_2$ membranes offer 4 orders of magnitude improvement in ionic conductivity compared to pristine γ-$LiAlO_2$. This is ascribed to the decreases in the Li^+ migration barrier by incorporating a 3D percolating network through the introduction of extrinsic defects and $LiAl_5O_8$. Long-term cycling of the Li/$Li_{3.1}AlO_2$/Li symmetric cell indicates that the membrane is stable with metallic Li at current densities of 0.375 mA cm^{-2}.

■ ASSOCIATED CONTENT

Supporting Information

The Supporting Information is available free of charge at https://pubs.acs.org/doi/10.1021/acsami.0c13021.

Supplemental analytical methods, crystallite size analysis, thermal stability of the green film, and EIS data (PDF)

■ AUTHOR INFORMATION

Corresponding Author

Richard M. Laine − *Department of Materials Science and Engineering, University of Michigan, Ann Arbor, Michigan 48109-2136, United States;* orcid.org/0000-0003-4939-3514; Phone: +1 734 764 6203; Email: talsdad@umich.edu; Fax: +1 734 763 4788

Authors

Eleni Temeche − *Department of Materials Science and Engineering, University of Michigan, Ann Arbor, Michigan 48109-2136, United States*

Sylvio Indris − *Institute for Applied Materials, Karlsruhe Institute of Technology, D-76344 Eggenstein-Leopoldshafen, Germany;* orcid.org/0000-0002-5100-113X

Complete contact information is available at: https://pubs.acs.org/10.1021/acsami.0c13021

https://dx.doi.org/10.1021/acsami.0c13021
ACS Appl. Mater. Interfaces 2020, 12, 46119−46131

Author Contributions

The manuscript was written with contributions from all authors.

Notes

The authors declare no competing financial interest.

■ ACKNOWLEDGMENTS

We are grateful for the support of a significant portion of this work by DOE through Batt500 Seedling project DE-EE0008235 and a gift from Mercedes-Benz Research & Development North America (MBRDNA). A portion of this work was also supported by a DMR NSF grant no. DMR project 1926199. We also like to thank the University of Michigan Rackham Merit Fellowship (RMF) program. We would like to thank Kayla Byrd, Nicole Wang, Yi Qiu, Dhruv Tatke, Hailey Kuntz, Taylor G. Brandt, and Thomas Gabrielson for their contributions.

■ REFERENCES

(1) Goodenough, J. B.; Kim, Y. Challenges for Rechargeable Batteries. *J. Power Sources* **2011**, 6688.

(2) Tarascon, J. M.; Armand, M. Issues and Challenges Facing Rechargeable Lithium Batteries. In *Materials for Sustainable Energy: A Collection of Peer-Reviewed Research and Review Articles from Nature Publishing Group*; 2010. DOI: 10.1142/9789814317665_0024.

(3) Manthiram, A.; Yu, X.; Wang, S. Lithium Battery Chemistries Enabled by Solid-State Electrolytes. *Nat. Rev. Mater.* **2017**, *2*, 16103.

(4) Fergus, J. W. Ceramic and Polymeric Solid Electrolytes for Lithium-Ion Batteries. *J. Power Sources* **2010**, 4554.

(5) Murugan, R.; Thangadurai, V.; Weppner, W. Fast Lithium Ion Conduction in Garnet-Type Li7$La_3Zr_2O_{12}$. *Angew. Chem., Int. Ed.* **2007**, 7778.

(6) Hu, Y.; Ruud, A.; Miikkulainen, V.; Norby, T.; Nilsen, O.; Fjellvåg, H. Electrical Characterization of Amorphous $LiAlO_2$ Thin Films Deposited by Atomic Layer Deposition. *RSC Adv.* **2016**, *6*, 60479−60486.

(7) Yi, E.; Wang, W.; Kieffer, J.; Laine, R. M. Flame Made Nanoparticles Permit Processing of Dense, Flexible, Li^+ Conducting Ceramic Electrolyte Thin Films of Cubic-$Li_7La_3Zr_2O_{12}$ (c-LLZO). *J. Mater. Chem. A* **2016**, *4*, 12947−12954.

(8) Fu, K. K.; Gong, Y.; Liu, B.; Zhu, Y.; Xu, S.; Yao, Y.; Luo, W.; Wang, C.; Lacey, S. D.; Dai, J.; Chen, Y.; Mo, Y.; Wachsman, E.; Hu, L. Toward Garnet Electrolyte−Based Li Metal Batteries: An Ultrathin, Highly Effective, Artificial Solid-State Electrolyte/Metallic Li Interface. *Sci. Adv.* **2017**, No. e1601659.

(9) Yi, E.; Wang, W.; Mohanty, S.; Kieffer, J.; Tamaki, R.; Laine, R. M. Materials That Can Replace Liquid Electrolytes in Li Batteries: Superionic Conductivities in Li1.7Al0.3Ti1.7Si 0.4P2.6O12. Processing Combustion Synthesized Nanopowders to Free Standing Thin Films. *J. Power Sources* **2014**, *269*, 577−588.

(10) Kwon, W. J.; Kim, H.; Jung, K. N.; Cho, W.; Kim, S. H.; Lee, J. W.; Park, M. S. Enhanced Li^+ Conduction in Perovskite $Li_{3X}La_{2/3-X}\square_{1/3-2x}TiO_3$ Solid-Electrolytes via Microstructural Engineering. *J. Mater. Chem. A* **2017**, 6257.

(11) Monchak, M.; Hupfer, T.; Senyshyn, A.; Boysen, H.; Chernyshov, D.; Hansen, T.; Schell, K. G.; Bucharsky, E. C.; Hoffmann, M. J.; Ehrenberg, H. Lithium Diffusion Pathway in Li1.3Al0.3Ti1.7(PO4)3 (LATP) Superionic Conductor. *Inorg. Chem.* **2016**, 2941.

(12) Han, X.; Gong, Y.; Fu, K.; He, X.; Hitz, G. T.; Dai, J.; Pearse, A.; Liu, B.; Wang, H.; Rubloff, G.; Mo, Y.; Thangadurai, V.; Wachsman, E. D.; Hu, L. Negating Interfacial Impedance in Garnet-Based Solid-State Li Metal Batteries. *Nat. Mater.* **2017**, 572.

(13) Arbi, K.; Rojo, J. M.; Sanz, J. Lithium Mobility in Titanium Based Nasicon Li1+xTi2-XAlx(PO4)3 and LiTi2-x Zrx(PO4)3 Materials Followed by NMR and Impedance Spectroscopy. *J. Eur. Ceram. Soc.* **2007**, 4215.

(14) Rangasamy, E.; Wolfenstine, J.; Sakamoto, J. The Role of Al and Li Concentration on the Formation of Cubic Garnet Solid Electrolyte of Nominal Composition $Li_7La_3Zr_2O_{12}$. *Solid State Ionics* **2012**, 28.

(15) Liu, W.-Y.; Fu, Z.-W.; Li, C.-L.; Qin, Q.-Z. Lithium Phosphorus Oxynitride Thin Film Fabricated by a Nitrogen Plasma-Assisted Deposition of E-Beam Reaction Evaporation. *Electrochem. Solid-State Lett.* **2004**, J36.

(16) Park, J. S.; Meng, X.; Elam, J. W.; Hao, S.; Wolverton, C.; Kim, C.; Cabana, J. Ultrathin Lithium-Ion Conducting Coatings for Increased Interfacial Stability in High Voltage Lithium-Ion Batteries. *Chem. Mater.* **2014**, *26*, 3128−3134.

(17) Choi, H. J.; Lee, J. J.; Hyun, S. H.; Lim, H. C. Phase and Microstructural Stability of Electrolyte Matrix Materials for Molten Carbonate Fuel Cells. *Fuel Cells* **2010**, 613.

(18) Chou, M. M. C.; Chang, L.; Chen, C.; Yang, W. F.; Li, C. A.; Wu, J. J. Growth Behavior of Nonpolar GaN on the Nearly Lattice-Matched (1 0 0) γ-$LiAlO_2$ Substrate by Chemical Vapor Deposition. *J. Cryst. Growth* **2009**, 448.

(19) Dai, Y. M.; Wu, J. S.; Chen, C. C.; Chen, K. T. Evaluating the Optimum Operating Parameters on Transesterification Reaction for Biodiesel Production over a LiAlO2 Catalyst. *Chem. Eng. J.* **2015**, 370.

(20) Morita, M.; Fujisaki, T.; Yoshimoto, N.; Ishikawa, M. Ionic Conductance Behavior of Polymeric Composite Solid Electrolytes Containing Lithium Aluminate. *Electrochim. Acta* **2001**, 1565.

(21) Zhu, B.; Liu, N.; McDowell, M.; Jin, Y.; Cui, Y.; Zhu, J. Interfacial Stabilizing Effect of ZnO on Si Anodes for Lithium Ion Battery. *Nano Energy* **2015**, 620.

(22) Sun, S.; Du, C.; Qu, D.; Zhang, X.; Tang, Z. Li_2ZrO_3-Coated $LiNi_{0.6}Co_{0.2}Mn_{0.2}O_2$ for High-Performance Cathode Material in Lithium-Ion Battery. *Ionics* **2015**, 2091.

(23) Ovalle-Encinia, O.; Pfeiffer, H.; Fabián-Anguiano, J. A.; Ortiz-Landeros, J. Nanosized Lithium Aluminate (γ-LiAlO2) Synthesized by EDTA-Citrate Complexing Method, Using Different Thermal Conditions. *J. Mex. Chem. Soc.* **2019**, DOI: 10.29356/jmcs.v63i4.1030.

(24) Cheng, J.; Guo, L.; Xu, S.; Zhang, R.; Li, C. Submicron γ-$LiAlO_2$ Powder Synthesized from Boehmite. *Chin. J. Chem. Eng.* **2012**, 776.

(25) Xu, X.; Wen, Z.; Lin, J.; Li, N.; Wu, X. An Aqueous Gel-Casting Process for γ-LiAlO2 Ceramics. *Ceram. Int.* **2010**, 187.

(26) Wen, Z.; Gu, Z.; Xu, X.; Zhu, X. Research on the Preparation, Electrical and Mechanical Properties of γ-LiAlO2 Ceramics. *J. Nucl. Mater.* **2004**, 1283.

(27) Miikkulainen, V.; Nilsen, O.; Li, H.; King, S. W.; Laitinen, M.; Sajavaara, T.; Fjellvåg, H. Atomic Layer Deposited Lithium Aluminum Oxide: (In)Dependency of Film Properties from Pulsing Sequence. *J. Vac. Sci. Technol., A* **2015**, 01A101.

(28) Utke, I.; Hoffmann, P.; Melngailis, J. Gas-Assisted Focused Electron Beam and Ion Beam Processing and Fabrication. *J. Vac. Sci. Technol., B* **2008**, 1197.

(29) Zhao, S.; Fu, Z.; Qin, Q. A Solid-State Electrolyte Lithium Phosphorus Oxynitride Film Prepared by Pulsed Laser Deposition. *Thin Solid Films* **2002**, *415*, 108−113.

(30) Zhang, X.; Temeche, E.; Laine, R. M. Design, Synthesis, and Characterization of Polymer Precursors to Li XPON and Li_XSiPON Glasses: Materials That Enable All-Solid-State Batteries (ASBs). *Macromolecules* **2020**, *53*, 2701−2712.

(31) Park, Y. J.; Kim, J. G.; Kim, M. K.; Chung, H. T.; Um, W. S.; Kim, M. H.; Kim, H. G. Fabrication of LiMn2O4 Thin Films by Sol-Gel Method for Cathode Materials of Microbattery. *J. Power Sources* **1998**, 41.

(32) Dudney, N. J. Thin Film Micro-Batteries. *Electrochem. Soc. Interface* **2008**, *17*, 44.

(33) Patil, V.; Patil, A.; Choi, J. W.; Lee, Y. P.; Yoon, Y. S.; Kim, H. J.; Yoon, S. J. LiCoO2 Thin Film Cathodes Grown by Sol-Gel Method. *J. Electroceram.* **2009**, 214.

(34) Lee, S. H.; Liu, P.; Tracy, C. E. Lithium Thin-Film Battery with a Reversed Structural Configuration SS/Li/Lipon/$Li_xV_2O_5$/Cu. *Electrochem. Solid-State Lett.* **2003**, A275.
(35) Takeuchi, M.; Niedermaier, M.; Jansohn, M.; Umehara, N.; Laine, R. M. Processing Thin (<10 μm), Dense, Flexible α-Al_2O_3 Films from Nanopowders. *J. Ceram. Soc. Japan* **2019**, *127*, 81−89.
(36) Bates, J. B.; Dudney, N. J.; Gruzalski, G. R.; Zuhr, R. A.; Choudhury, A.; Luck, C. F.; Robertson, J. D. Fabrication and Characterization of Amorphous Lithium Electrolyte Thin Films and Rechargeable Thin-Film Batteries. *J. Power Sources* **1993**, *43*, 103−110.
(37) Wohlmuth, D.; Epp, V.; Bottke, P.; Hanzu, I.; Bitschnau, B.; Letofsky-Papst, I.; Kriechbaum, M.; Amenitsch, H.; Hofer, F.; Wilkening, M. Order vs. Disorder - A Huge Increase in Ionic Conductivity of Nanocrystalline $LiAlO_2$ Embedded in an Amorphous-like Matrix of Lithium Aluminate. *J. Mater. Chem. A* **2014**, 20295.
(38) Temeche, E.; Yi, E.; Keshishian, V.; Kieffer, J.; Laine, R. M. Liquid-Feed Flame Spray Pyrolysis Derived Nanopowders (NPs) as a Route to Electrically Conducting Calcium Aluminate (12CaO.7Al2O3) Films. *J. Eur. Ceram. Soc.* **2019**, *39*, 1263−1270.
(39) Yi, E.; Temeche, E.; Laine, R. M. Superionically Conducting B″-Al2O3thin Films Processed Using Flame Synthesized Nanopowders. *J. Mater. Chem. A* **2018**, *6*, 12411−12419.
(40) Imagawa, H.; Ohta, S.; Kihira, Y.; Asaoka, T. Garnet-Type Li6.75La3Zr1.75Nb 0.25O12 Synthesized by Coprecipitation Method and Its Lithium Ion Conductivity. *Solid State Ionics* **2014**, 609.
(41) Chen, G.; Fu, Y. F.; Hu, K. A.; Zhang, D. Preparation of $LiAlO_2$ Powders for the Electrolyte Matrix Material. *J. Shanghai Jiaotong Univ.* **2003**, 260.
(42) Ouahdi, N.; Guillemet, S.; Durand, B.; Ouatib, R. E.; Rakho, L. E.; Moussa, R.; Samdi, A. Synthesis of CoAl2O4 by Double Decomposition Reaction between LiAlO2 and Molten KCoCl3. *J. Eur. Ceram. Soc.* **2008**, 1987.
(43) Marezio, M. The Crystal Structure and Anomalous Dispersion of γ-LiAlO 2. *Acta Crystallogr.* **1965**, 396.
(44) Chou, M. M. C.; Chun Tsao, P.; Chun Huang, H. Study on Czochralski Growth and Defects of LiAlO2 Single Crystals. *J. Cryst. Growth* **2006**, 542.
(45) Wiedemann, D.; Nakhal, S.; Rahn, J.; Witt, E.; Islam, M. M.; Zander, S.; Heitjans, P.; Schmidt, H.; Bredow, T.; Wilkening, M.; Lerch, M. Unravelling Ultraslow Lithium-Ion Diffusion in γ-LiAlO2: Experiments with Tracers, Neutrons, and Charge Carriers. *Chem. Mater.* **2016**, 915.
(46) Laine, R. M.; Marchal, J.; Sun, H.; Pan, X. Q. A New Y3Al5O12 Phase Produced by Liquid-Feed Flame Spray Pyrolysis (LF-FSP). *Adv. Mater.* **2005**, *17*, 830−833.
(47) Yi, E.; Wang, W.; Kieffer, J.; Laine, R. M. Key Parameters Governing the Densification of Cubic-Li7La3Zr2O12 Li+ Conductors. *J. Power Sources* **2017**, 156.
(48) Irfan, H.; Mohamed Racik, K.; Anand, S. Microstructural Evaluation of $CoAl_2O_4$ Nanoparticles by Williamson−Hall and Size−Strain Plot Methods. *J. Asian Ceram. Soc.* **2018**, 54.
(49) Williamson, G. K.; Hall, W. H. X-Ray Line Broadening from Filed Aluminium and Wolfram. *Acta Metall.* **1953**, 22.
(50) Scherrer, P. Bestimmung Der Größe Und Der Inneren Struktur von Kolloidteilchen Mittels Röntgenstrahlen.In *Kolloidchemie Ein Lehrbuch;* Springer, 1912.
(51) Kr Kalita, A.; Karmakar, S. Synthesis and Structural Characteristics of Fe Doped ZnO Nanoparticles at Different Molarities and Temperatures. *J. Nanosci. Technol.* **2019**, 645.
(52) *Advanced Processing and Manufacturing Technologies for Structural and Multifunctional Materials*; 2007. DOI: 10.1002/9780470339718.
(53) Issac, I.; Heinzmann, R.; Becker, S. M.; Bräuniger, T.; Zhao-Karger, Z.; Adelhelm, C.; Kiran Chakravadhanula, V. S.; Kübel, C.; Ulrich, A. S.; Indris, S. Synthesis of Nanocrystalline Solid Solutions AlySn 1-YO2-y/2 (y = 0.57, 0.4) Investigated by XRD, 27Al/119Sn MAS NMR, and Mössbauer Spectroscopy. *RSC Adv.* **2012**, DOI: 10.1039/c2ra21540c.
(54) Bräuniger, T.; Jansen, M. Solid-State NMR Spectroscopy of Quadrupolar Nuclei in Inorganic Chemistry. *Z. Anorg. Allg. Chem.* **2013**, 857.
(55) Mo, S.; Zhang, B.; Zhang, K.; Li, S.; Pan, F. $LiAl_5O_8$ as a Potential Coating Material in Lithium-Ion Batteries: A First Principles Study. *Phys. Chem. Chem. Phys.* **2019**, 13758.
(56) Islam, M. M.; Bredow, T. Interstitial Lithium Diffusion Pathways in γ-LiAlO2: A Computational Study. *J. Phys. Chem. Lett.* **2015**, 4622.
(57) Falco, M.; Ferrari, S.; Appetecchi, G. B.; Gerbaldi, C. Managing Transport Properties in Composite Electrodes/Electrolytes for All-Solid-State Lithium-Based Batteries. *Mol. Syst. Design Eng.* **2019**, 850.
(58) Han, J. H.; Kim, D. Y. Determination of Three-Dimensional Grain Size Distribution by Linear Intercept Measurement. *Acta Mater.* **1998**, 2021.
(59) KONISHI, S.; OHNO, H. Electrical Conductivity of Polycrystalline Li_2SiO_3 and Γ-$LiAlO_2$. *J. Am. Ceram. Soc.* **1984**, *67*, 418−419.
(60) Park, M.; Zhang, X.; Chung, M.; Less, G. B.; Sastry, A. M. A Review of Conduction Phenomena in Li-Ion Batteries. *J. Power Sources* **2010**, 7904.
(61) Indris, S.; Heitjans, P.; Uecker, R.; Roling, B. Li Ion Dynamics in a $LiAlO_2$ Single Crystal Studied by 7Li NMR Spectroscopy and Conductivity Measurements. *J. Phys. Chem. C* **2012**, *116*, 14243−14247.
(62) Hu, Q.; Lei, L.; Jiang, X.; Feng, Z. C.; Tang, M.; He, D. Li Ion Diffusion in $LiAlO_2$ Investigated by Raman Spectroscopy. *Solid State Sci.* **2014**, 103.
(63) Glass, A. M.; Nassau, K. Lithium Ion Conduction in Rapidly Quenched Li_2O-Al_2O_3, Li_2O-Ga_2O_3, and Li_2O-Bi_2O_3 Glasses. *J. Appl. Phys.* **1980**, 3756.
(64) Temeche, E.; Zhang, X.; Richard, M. L. Solid Electrolytes for Li-S Batteries: Solid Solutions of Polyethylene Oxide with Li_xPON and Li_xSiPON Based Polymers. **2020**, *12* (), 30353−30364.
(65) Temeche, E.; Zhang, X.; Laine, R. M. Polymer Precursor Derived LiXPON Electrolytes: Toward Li-S Batteries. *ACS Appl. Mater. Interfaces* **2020**, *12*, 20548−20562.
(66) Huang, S.; Wen, Z.; Zhu, X.; Lin, Z. Effects of Dopant on the Electrochemical Performance of Li4Ti5O12 as Electrode Material for Lithium Ion Batteries. *J. Power Sources* **2007**, 408.
(67) Zhang, J.; Zhang, J.; Cai, W.; Zhang, F.; Yu, L.; Wu, Z.; Zhang, Z. Improving Electrochemical Properties of Spinel Lithium Titanate by Incorporation of Titanium Nitride via High-Energy Ball-Milling. *J. Power Sources* **2012**, 133.